Science of the Total Environment 751 (2021) 142338

Contents lists available at ScienceDirect

Science of the Total Environment

journal homepage: www.elsevier.com/locate/scitotenv

Lateral flow between bald and vegetation patches induces the degradation of alpine meadow in Qinghai-Tibetan Plateau

Xiao-Jin Jiang [a,b], Xiai Zhu [a,b], Zi-Qiang Yuan [c], Xiao Gang Li [d], Wenjie Liu [a,b,*], Sissou Zakari [a,b,*]

[a] CAS Key Laboratory of Tropical Forest Ecology, Xishuangbanna Tropical Botanical Garden, Chinese Academy of Sciences, Menglun, Yunnan 666303, China
[b] Center of Plant Ecology, Core Botanical Gardens, Chinese Academy of Sciences, Menglun, Yunnan 666303, China
[c] State Key Laboratory of Frozen Soil Engineering, Northwest Institute of Eco-Environment and Resources, Chinese Academy of Sciences, Lanzhou 730000, China
[d] State Key Laboratory of Grassland and Agro-ecosystems, Institute of Arid Agroecology, School of Life Sciences, Lanzhou University, Lanzhou 730000, China

HIGHLIGHTS

- Bald patches (BPs) are the precursors of alpine meadows degradation.
- Mattic epipedon layer of vegetation patches (VPs) reduces soil permeability.
- VPs produce high runoff during rainfall, then BPs accept this runoff.
- Lateral flow affects the process of freezing-thawing, frost heaves, and thaw slump.
- Marginal meadow at the interface between BPs and VPs is easily eroded and detached.

GRAPHICAL ABSTRACT

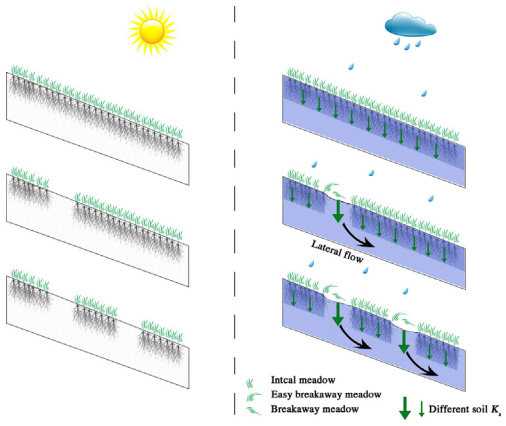

ARTICLE INFO

Article history:
Received 22 June 2020
Received in revised form 8 September 2020
Accepted 8 September 2020
Available online 10 September 2020

Editor: Fernando A.L. Pacheco

Keywords:
Active layers
Lateral flow
Saturated hydraulic conductivity
Soil erosion
Desertification
High desert and cold systems

ABSTRACT

Bald patches (BPs) are known to accelerate and simultaneously mitigate the process of desertification. However, the mechanisms of these two synchronous actions are little studied in high desert and cold systems; and the incidence of BPs on alpine meadows degradation in Qinghai-Tibetan Plateau (QTP) of China is still unavailable. This study first aims to investigate the soil properties and the erodibility of the system BPs-VPs at the Beiluhe basin in QTP. Then, we adopted dye tracer and HYDRUS-2/3D methods to interpret the water infiltration patterns from point scale to slope scale. The results show that the mattic epipedon layer on the top soil (0–20 cm) of VPs directly reduced the impact of raindrops on alpine meadow; and the adhesion of root system in VPs prevented the soil particles from stripping and washing away by runoff. The soil particles in BPs were easily eroded by rainfall, lowering the ground level of BPs relative to the ground level of VPs. The two patches therefore alternated to form an erosion interface where marginal meadow was likely detached by raindrops, and washed away through runoff. The saturated hydraulic conductivity (K_s) of surface soil (0–10 cm) was 124% higher in BPs than the VPs. Thereby, BPs caused a high spatial variation of infiltration and runoff in QTP. Moreover, this difference in K_s between the two patches conducted to a lateral flow from BPs to VPs, and to soil layers with different water contents. These findings highlight that the water flow features can potentially disturb the processes of freezing-thawing, frost heaves, and thaw slump; and accelerate the alpine meadow degradation. Therefore, land cover such as crop and vegetation should be applied over the bare soil surface to prevent the degradation of alpine meadow.

* Corresponding authors at: CAS Key Laboratory of Tropical Forest Ecology, Xishuangbanna Tropical Botanical Garden, Chinese Academy of Sciences, Menglun, Yunnan 666303, China.
E-mail addresses: lwj@xtbg.org.cn (W. Liu), sissouzakari@xtbg.ac.cn (S. Zakari).

https://doi.org/10.1016/j.scitotenv.2020.142338
0048-9697/

1. Introduction

Bare soil areas interspersed among vegetation (hereafter VPs) are common features in arid and semiarid zones (Barberá et al., 2007; Kakembo et al., 2012). These bare soil areas, referred to as bald patches, or BPs, play a dual role in desertification (accelerate and mitigate desertification). Bald patches support the formation of biological and physical crusts (Assouline et al., 2015). The biological activities (e.g., root growth and termite digging) in BPs create macropores (Guebert and Gardner, 2001) that enhances water infiltration at the expense of surface runoff (Barger et al., 2006; Belnap, 2006; Issa et al., 2011). Alternatively, the physical soil crusts in BPs reduce water infiltration capacity, and exacerbate water stress on the remaining vegetation (Belnap, 2006; Thompson et al., 2010). The mechanisms leading to this dual role of BPs have been previously studied in the context of arid and semi-arid environments (Belnap, 2006; Thompson et al., 2010; Assouline et al., 2015). However, little research has been conducted to understand these mechanisms in high desert and cold systems, despite the prevalence of BPs (Barger et al., 2006; Itzhak et al., 2007; Li et al., 2008) and the increasing degradation of these systems (Harris, 2010; Wen et al., 2010; Chen et al., 2017).

Alpine meadow in the QTP is representative of high-alpine and cold systems. It is characterized by three distinct features which are important for its ecosystems grassland succession: a mattic epipedon layer (Zeng et al., 2013), a heterogeneous rainfall distribution (You et al., 2014), and an active permafrost layer (Zhao et al., 2004; Yin et al., 2017). These unique features lead to distinct ecohydrological processes (Wang et al., 2012). As a result, the theories on the role of BPS in arid and semi-arid environments may not be valid in high desert and cold environments. However, previous research provides insights into the complex effects of the above-mentioned three features on the distribution of water, nutrients, and sediment in the alpine meadow. For instance, the degradation of VPs can increase (Wang et al., 2007) or decrease (Cheng et al., 2008; Zeng et al., 2013) the soil saturated hydraulic conductivity (K_s). More, an uneven distribution of rainfall in the QTP throughout the year is found the trigger downcutting at ground levels of BPs to form headward erosion (Zeng et al., 2013). Finally, the active permafrost soil layer can undergo a melt-freeze process while the permanent frozen soil layer stays frozen throughout the year (Wen et al., 2010; Wang et al., 2012; Chen et al., 2017). Thus, the late freezing process would be affected by flowing rainwater into the active permafrost layer during melting process.

Such above mentioned features can accelerate the degradation of alpine meadow in the QTP. They can also contribute to the expansion of BPs through the destruction of the mattic epipedon layer at the interface between BPs and VPs (Harris, 2010; Wen et al., 2010; Chen et al., 2017), to form desertification lands and thermokarst lakes (Wang et al., 2018). However, few studies have investigated the interaction between these three unique features and the formation of BPs, the subsequent effects of BPs on QTP lands desertification, and the occurrence of thermokarst lakes. Thus, knowing the contribution of BPs on the degradation of alpine meadows is urgently required, considering the special geographical location of the QTP, and the impacts of this latter on ecology, hydrology, climate and environment (You et al., 2014; Wang et al., 2018).

The present research aims to (1) evaluate the effects of BPs on QTP soil properties. Then, it (2) determines the dominant water flow behavior at the interface between BPs and VPs using combined methods of dye tracer (at point scale) and HYDRUS-2/3D simulation (at slope scale). It also (3) evaluates the potential contribution of each soil layer on sediment yield, once the alpine meadow disappears from the soil surface exposing deeper soil layers to water erosion. We discussed and interpreted the results from this study in the broader context of high desert and cold systems. The findings exhibit the potential mechanisms of alpine meadow degradation, and a conceptual model for understanding the contribution of these mechanisms in the initial stage of QTP desertification and thermokarst lakes. This study is an important contribution to the knowledge on the degradation of alpine meadows.

2. Materials and methods

2.1. General methodology

This study used a combination of methods to investigate the questions highlighted in each objective (Fig. 1 A, B, C). We measured in both BPs and VPs the soil K_s and soil properties concerning initial water content, capillary porosity, noncapillary porosity, field capacity, saturated water-holding capacity, soil organic carbon (SOC), particle size, and root biomass. Moreover, dye-tracer infiltration experiments at point scale and HYDRUS 2–3/D modelling at slope scale was used to illustrate and interpret the dominant water flow behavior in the interface between BPs and VPs. Simulated rainfall erosion experiments were conducted on soil blocks, which were collected from soil layers of BPs and VPs, to determine the potential effect of each soil layer on sediment yield. Finally, we discussed and interpret the results of this study in the broader context of high desert and cold systems through a literature review.

2.2. Study site

The study site (34° 39′ N, 92° 55′ E; 4635 m asl) is located in Beiluhe basin in the "Three-River-Source National Park" on the QTP. The basin is in flat terrain with most slopes <10°. It is characterized by continental-monsoon with long severe winters and short cool summers. Based on a ten years (2002−2011) meteorological data from the Beiluhe Weather Station, the area mean annual, maximum, and minimum air temperatures are −3.8 °C, 19.2 °C, and − 27.9 °C, respectively. The mean annual precipitation at the study site is 290.9 mm (more than 95% falls during the warm season from April to October), and the mean annual evaporation is 1316.9 mm (You et al., 2014). Over 90% of precipitation falls between May and September when air temperatures remain above 0 °C. The mean annual potential evaporation is about 1317 mm yr^{-1}, much higher than the mean annual precipitation. The soil freezes from September to April of the next year. The soil of the study site is typically alpine meadow soil (or felty soil, comparable to FAO-UNESCO's cambisols) (Wang et al., 2008), with *Kobresia pygmaea* as dominant species (You et al., 2014).

Beiluhe basin is underlain with warm and ice-rich permafrost aquitard, which can become supra-permafrost water in the QTP (Cheng and Jin, 2013). The permafrost has a low permeability that blocks soil water infiltration and affects subsurface water flow, which combined with the infiltration processes are important for the redistribution of precipitation in the middle and lower slope regions (Pan et al., 2017). The degradation of permafrost can also enhance the hydrologic and hydrogeological connectivity (Grenier et al., 2013).

2.3. Plots installation and K_s measurements

Three replicate plots were randomly established in the study site (Fig. 1 A) between July 2018 and August 2018. Each plot was installed to obtain an interface between BPs (average vegetation cover was less to 5% ± 2.4%) and VPs (average vegetation cover was approximately 90% ± 6.6%) (Fig. 1 B). Six bulk soil samples (three on BPs and three on VPs) were taken in each plot at depths of 5, 15, 30, and 50 cm using volumetric rings (inner diameter: 70.00 mm, height: 52.00 mm, and volume: 200 cm^3). Given that the mattic epipedon layer was very compact and hard due to abundant roots entwined with each other, we applied a treatment during the soil collection to facilitate the insertion of the volumetric ring, as described in the following sentences. The volumetric ring was placed on the soil surface and its position was set to form a circular ring that divided the soil into two internal and external sub-regions. Then, we cut the roots connections between the two sub-regions, and inserted

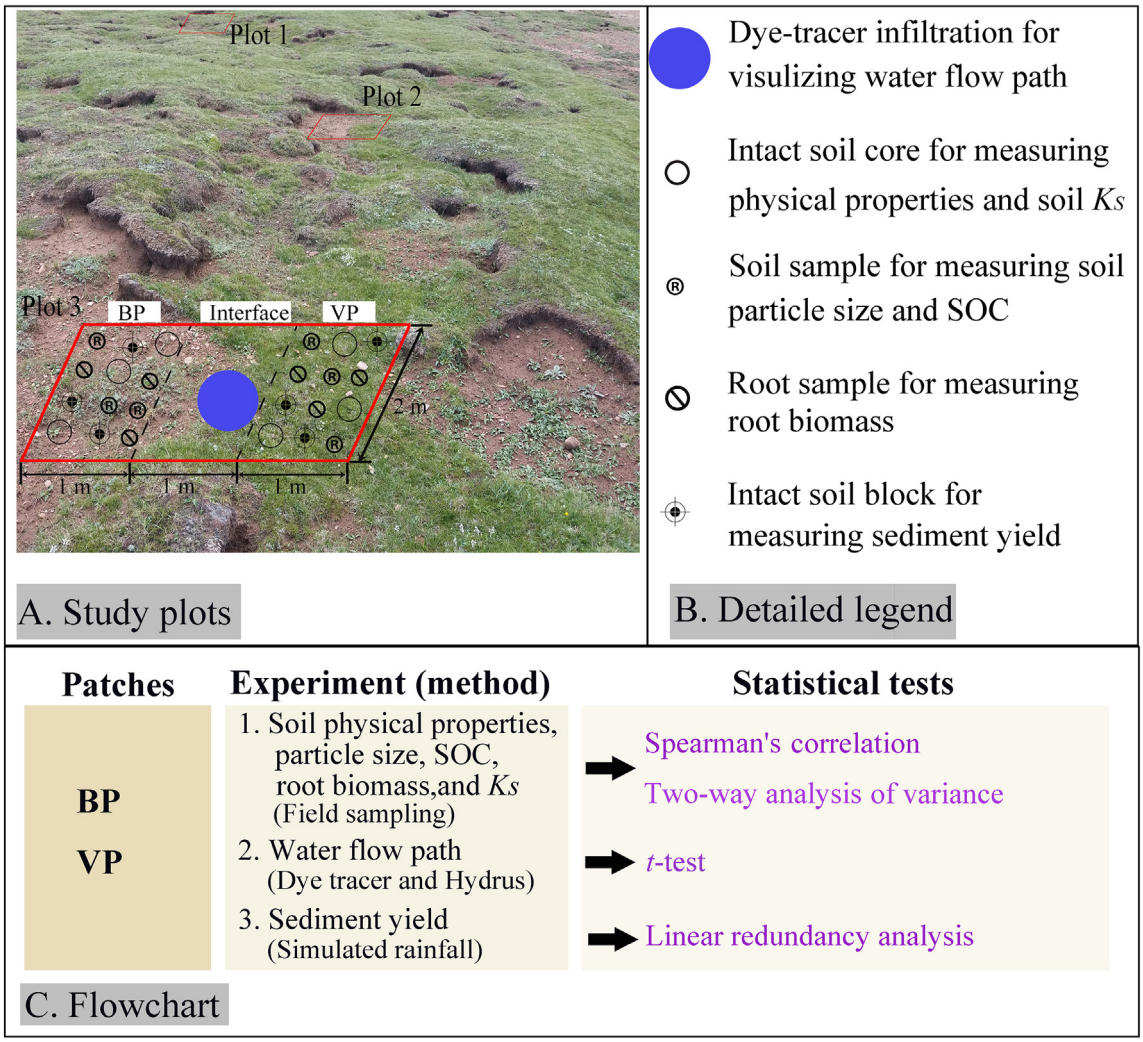

Fig. 1. Study site location (Beiluhe basin) in the Qinghai-Tibetan Plateau, China (You et al., 2014). Three plots (separated by more than 15 m) containing bald patches (BPs), vegetation patches (VPs), and the interface between the two patches were considered (A). In each plot (B), one dye-tracer infiltration was conducted at the centre axis of the interface, 24 intact soil cores and 24 intact soil blocks were collected at various depths of 5, 15, 30, and 50 cm in each plot of the BPs and VPs. The ground slope of the experimental site was <10°. Flowchart summarizing the general experiments, methods, and statistical tests of the present study (C).

the volumetric ring into the subsoil. We kept the volumetric ring in a stable position throughout the collection of intact soil cores.

The collected intact soil cores were first placed in a tray containing distilled water in laboratory for 24 h, then soil K_s was measured by mean of infiltration method using a designed infiltration apparatus (per Jiang et al., 2017). To measure K_s, the top cover of the volumetric ring (containing the soil column) was removed and replaced by a circular wire mesh. Then, a hollow volumetric ring was spliced on the top of the ring containing soil column, and poured with distilled water. A burette was used to ensure that the water level was as high as the height of the volumetric ring, and a small cup was placed at the bottom of the volumetric ring containing the soil column to collect the outflow.

During the infiltration experiment, the infiltration and outflow volumes were recorded each 2 min. The steady-state condition occurred when the rate of infiltration is similar to the rate of outflow. The steady-state infiltration rate (I_s, cm min^{-1}), which is the water passage per unit area per unit thickness per unit time, was calculated using the last five infiltration and outflow volumes (Bodhinayake et al., 2005). I_s was converted to K_s at 10 °C (Yang et al., 2017) using the formula in Eq. (2).

$$I_s = \frac{Q \times L}{t \times S \times (H + L)} \quad (1)$$

$$K_s = \frac{I_s}{0.7 + 0.03\,T} \quad (2)$$

where Q is the total amount of outflow (cm^3), L is the soil thickness (cm), S is the cross-sectional area of the volumetric ring (cm^2), H is the height of the volumetric ring (cm), t is the recorded time (min), T is the water temperature in field (°C).

2.4. Measurement of soil properties

Soil physical properties are critical parameters affecting its hydrological properties, and they are typically used to simulate and understand soil characteristics. The soil physical properties were determined using soil cores recovered from K_s experiments. Soil effective saturation was measured using the volumetric rings (containing intact soil cores) placed in a tray containing distilled water. We estimated initial water content, bulk density, capillary porosity, noncapillary porosity, field capacity, and saturated water-holding capacity at 5, 15, 30, and 50 cm depths of BPs and VPs (per Zhu et al., 2019). The total porosity was estimated in intact water-saturated samples of 200 cm^3, assuming that air was not trapped in the soil pores, and confirmed using dry bulk density and particle density of 2.65 g cm^{-3} (Danielson and Sutherland, 1986).

Soil chemical properties and particle size were measured from bulk soils collected at depths of 5, 15, 30, and 50 cm in BPs and VPs using 5.0 cm diameter auger. The SOC was determined by elemental analyzer (Elementar Analysensysteme GmbH, German) after air drying the soil samples at room temperature (20 °C). The particle size was measured using a Malvern Mastersizer 3000 laser particle size analyzer, combined with a Hydro 2000MU pump accessory (Malvern Instruments Ltd., Worcestershire, UK). As has advised Per Miller and Schaetzl (2012), we used a soil refractive index and absorption value of 1.549 and 0.01, respectively. Distilled water was used as dispersant and was assumed to have a refractive index of 1.33. In addition, the root biomass was determined from soil samples collected at 5, 15, 30, and 50 cm depths of BPs and VPs using root sampler (inner diameter, 25 mm; height, 150 mm). The roots were first gathered after sieving (2 mm mesh) and washing the soil, then they were dried in the oven at 80 °C to constant weight.

2.5. Dye-tracer infiltration

Three dye-tracer infiltrations were carried out at the interface between BPs and VPs using the following procedure. The surface vegetation and a thin layer of the soil (less than 2.0 cm) were carefully removed to ensure a horizontal surface; and the infiltration hollow stainless-steel cylinder (single-ring infiltrometer) was inserted at 5 cm soil depth. The side walls and edges of the cylinder were watertight. Each cylinder (diameter: 0.2 m, height: 0.3 m) was filled with 42 L of water dye solution containing 4.0 g L^{-1} Brilliant Blue FCF dye tracer (Flury and Flühler, 1995) to conduct the tracing infiltration experiment.

After the infiltration experiments, the wetted area of each plot was covered with a vinyl film to prevent external water input, and we dug a vertical section at each interface centre 24 h after the end of the infiltration experiment. Then, a pit (length: 100.0 cm, width: 60.0 cm, height: 70.0 cm) was excavated in front of the vertical soil sections, to support a digital camera (Canon EOS Rebel T3, Japan) at the distance of 50 cm from the front and 50 cm from the bottom. Frames (height, 30.0 cm; width, 50.0) were placed at right angles along the vertical sides of each profile to provide further geometric correction, and a black umbrella was used to provide soft light during the camera shot of the soil profiles.

Three dye-stained calibration patches were prepared to define the concentration ranges (0.05–0.5, 0.5–2.0, and > 2.0 g L^{-1}) of the obtained images (Weiler and Flühler, 2004) on the basis of dye-stained intensity using the Earth Resources Data Analysis System (ERDAS) IMAGINE version 9.0 (per Forrer et al., 2000; Cey and Rudolph, 2009). We subsequently performed on each image a geometric correction, background subtraction, colour adjustment, histogram stretching, image classification, and visual check. Then, the area of each concentration range was estimated through the value of stained pixels in the dye-staining patterns (per Jiang et al., 2015).

After the soil profiles shots, the area of each profile was subdivided into grids (1.5 cm × 1.5 cm) to collect soil samples (height, 1.5 cm; width, 1.5 cm; thickness, 1.0 cm), which are used to determine soil gravimetric water content. In total, 1215 soil samples were collected from each profile (width, 60.0 cm; depth, 55.0 cm). Moreover, the outer surface of each sample was cut to a thickness of 1.0 to avoid the impact of climatic factors. Finally, the obtained soil samples were transported into plastic bag (width, 5.0 cm; depth, 5.0 cm; thickness, 0.25 cm) to the laboratory for further analysis.

2.6. HYDRUS-2/3D subsoil water flow simulation

We used the HYDRUS 2–3/D software package (version 2.03) (Šimůnek et al., 2006, 2016) to simulate soil water movement processes across different ratios of VPs and BPs in the 20 cm (matching the root depth) of soil in the experimental plots, using a model domain of 400 cm^2. We selected an atmospheric boundary layer for the upper boundary condition, to which precipitation was applied, and we applied a 'no flux' lower boundary condition. The left and right boundary condition were set as free drainage conditions, the evaporation rate is assumed negligible, and the initial water contents are assumed uniform across the flow domain. Then, the model was simulated with a time step of 1 h. The HYDRUS-2/3D outputs were used to compute and visualize the subsoil flow across various BPs/VPs configurations (m, 100% VPs; n, 80% VPs and 20% BPs; o, 60% VPs and 40% BPs; p, 40% VPs and 60% BPs; q, 20% VPs and 80% BPs). Finally, the subsoil volumetric water content was estimated from HYDRUS-2/3D outputs, in ranges similar to those of the dye patterns, and compared with observed volumetric water content of the field infiltration experiments.

Assuming a homogeneous and isotropic soil, the governing two-dimensional flow is described by the Richards equation (Celia et al., 1990), and the equation is solved by the Galerkin finite-element method:

$$\frac{\partial \theta}{\partial t} = \frac{\partial}{\partial \chi}\left[K(h)\frac{\partial h}{\partial \chi}\right] + \frac{\partial}{\partial z}\left[K(h)\frac{\partial h}{\partial z}\right] + \frac{\partial K(h)}{\partial z} \tag{3}$$

where θ is the saturated water content ($cm^3\ cm^{-3}$), t is the time (min), x is the horizontal coordinate (cm), z is the vertical coordinate that is positive upward (cm), h is the pressure head (cm), and $K(h)$ is the unsaturated hydraulic conductivity (cm min^{-1}).

The soil water retention, $\theta(h)$, and hydraulic conductivity, $K(h)$, were described using the analytical functions of van Genuchten (1980) as follows:

$$\theta(h) = \begin{cases} \theta_1 + \dfrac{\theta_s - \theta_r}{\left[1 + |\alpha h|^n\right]^{1-1/n}} & h < 0 \\ \theta_5 & h \geq 0 \end{cases} \tag{4}$$

$$K(h) = K_s S_e^l \left\{1 - \left[1 - S_e^{n/(n-1)}\right]^{1-1/n}\right\}^2 \tag{5}$$

where S_e is effective saturation:

$$S_e = \frac{\theta(h) - \theta_r}{\theta_s - \theta_r} \tag{6}$$

and where θ_s is the saturated water content ($cm^3\ cm^{-3}$), θ_r is the residual water content ($cm^3\ cm^{-3}$), K_s is the saturated hydraulic conductivity (cm min^{-1}), α is the air entry parameter (cm^{-1}), n is the pore size distribution parameter, and l is the pore connectivity parameter. Parameters α, n, and l are empirical coefficients that determine the shape of hydraulic functions. The van Genuchten hydraulic function parameters (θ_r, α, n, and l) were estimated using the Neural Network Function in Rosetta (Schaap et al., 2001) with soil texture (sand, silt and clay fractions) and soil bulk density as input variables, and the other two hydraulic parameters (K_s is and θ_s) were from our field data (Table 1).

2.7. Simulated rainfall erosion experiment

Three replicates of 200 g intact soil blocks were collected in each soil plot at of 5, 15, 30, and 50 cm depths. The abundant roots of the root zone (about 15 cm depth) were cut off in the boundaries to obtain intact soil blocks, which were wrapped with plastic film and carefully transported to the laboratory to produce new-cube soil sub-blocks (100 g). Then, the sediment yield was measured from the soil sub-blocks under simulated rainfall using a Meyer style rainfall simulator (Meyer and Harmon, 1984). The sprinkling pipe of the rainfall simulator (3 m long) was installed horizontally at 2 m above the ground, and set to spray an area of 3 m × 3 m through a back and forth swivelling. A basin collector (50 cm diameter) containing 100 g intact soil was placed under the scope to erode the intact soil with a spraying intensity of 10 mm min^{-1}. This rain intensity was slightly higher than those of the

Table 1
Variation of soil properties (mean ± SE, $n = 9$) between bald patches (BPs) and vegetation patches (VPs) at different soil depth. K_S: saturated hydraulic conductivity; SOC: soil organic carbon.

Depth (cm)	Plot	Initial gravimetric water content (%)	Root biomass (g m^{-2})	Bulk density (g cm^{-3})	Noncapillary porosity (%)	Capillary porosity (%)	Field capacity (%)	Saturated water-holding capacity (%)	K_s (cm day^{-1})	SOC (g kg^{-1})	Particle size		
											Clay (%)	Silt (%)	Sand (%)
0–10	VPs	21.85(0.48)	2653.2 (11.29)	1.16(0.01)	5.15(0.38)	49.39 (1.83)	37.54 (3.72)	46.82(1.58)	13.92(1.73)	30.9 (1.11)	3.7 (0.18)	48.0 (0.46)	48.3 (0.29)
	BPs	12.43(0.71)	1628.2 (15.11)	1.39(0.02)	4.37(0.55)	45.33 (2.23)	25.78 (2.22)	35.81(1.96)	31.20(2.09)	17.9 (0.90)	2.0 (0.22)	32.6 (1.14)	65.4 (1.22)
10–20	VPs	16.51(0.96)	1416.4 (10.38)	1.17(0.05)	3.88(0.22)	50.43 (1.38)	33.58 (2.04)	46.50(2.65)	24.69(0.68)	29.7 (0.40)	3.8 (0.08)	46.6 (0.46)	49.6 (0.50)
	BPs	10.10(2.04)	1219.8 (6.45)	1.42(0.04)	4.49(0.71)	43.57 (2.79)	23.96 (3.79)	33.76(2.39)	29.28(1.73)	15.8 (0.92)	1.8 (0.06)	31.1 (0.92)	67.1 (0.98)
20–40	VPs	15.79(0.72)	800.1 (12.63)	1.30(0.04)	4.39(0.38)	48.26 (1.58)	27.48 (1.99)	40.51(1.99)	27.23(0.85)	20.3 (0.45)	3.2 (0.17)	43.4 (0.69)	53.4 (0.86)
	BPs	10.95(0.11)	791.3 (10.00)	1.54(0.05)	3.55(0.27)	41.74 (2.16)	22.47 (1.92)	29.55(2.13)	28.32(2.09)	12.7 (0.25)	3.4 (0.10)	40.0 (0.40)	56.6 (0.35)
40–60	VPs	13.68(0.93)	333.0 (13.74)	1.47(0.07)	3.49(0.59)	42.74 (5.08)	23.52 (4.08)	31.58(5.01)	28.80(0.83)	19.1 (0.84)	2.0 (0.06)	35.8 (0.42)	62.2 (0.37)
	BPs	11.94(0.30)	325.6 (9.69)	1.47(0.04)	3.69(0.67)	41.13 (0.96)	21.33 (1.13)	30.59(1.20)	29.28(2.54)	12.5 (0.58)	2.1 (0.07)	33.9 (0.64)	64.0 (0.67)
Summary of ANOVA (p values)													
Depth		<0.001	<0.001	<0.001	0.343	<0.001	<0.001	<0.001	<0.001	<0.001	<0.001	<0.001	<0.001
Plot		<0.001	<0.001	<0.001	<0.01	<0.01	<0.001	<0.001	<0.01	<0.001	<0.001	<0.001	<0.001
Depth × Plot		<0.001	<0.001	<0.001	0.057	0.284	<0.05	<0.01	<0.001	<0.001	<0.001	<0.001	<0.001

$LSD_{0.05}$ values within each bracket after the p values.

studied site, but it is the lowest intensity of our simulator. The sediment and water were directed to another basin using a pipe (diameter, 10 cm), and the content was collected every five mins for 40 mins. Finally, each 5 min collected sample was evaporated and oven dried at 105 °C for 24 h, and the remaining soil was weighted with an electronic balance to estimate the sediment yield (g).

2.8. Statistical analysis

Soil properties, root biomass, and sediment yields were first tested for normal distribution, and the non-normally distributed variables were log or square root transformed. Then, the two-way analysis of variance (ANOVA) test was applied to assess the effects of factors such as land type (BPs and VPs) and soil depth on the soil properties. Moreover, t-test was used to compare the dye-staining characteristics such as maximum dye-stained width, maximum dye-stained depth, and dark blue area; and the sediment yield between land types. Spearman's correlation was computed on the data to obtain the relationship between variables of soil property. All these analyses were computed using SPSS 20.0 (Statistical Package for Social Sciences, SPSS Inc., Chicago, IL, USA). Moreover, we applied linear redundancy analysis to explore the relationships between sediment yield and soil properties, and conducted Monte Carlo permutation test based on 499 random permutations to evaluate the significance of the canonical axes eigenvalues (ter Braak and Smilauer, 2002). Ordination analyses were performed with CANOCO 4.5.

3. Results

3.1. Soil properties in BPs and VPs

BPs significantly affected the QTP soil properties, which were in turn significantly influenced by soil depth only for the non-capillary porosity (Table 1). The difference in soil properties between BPs and VPs was mainly observed at the upper 20 cm of the soil profile. More than half of the root biomass was confined to the upper 20 cm soil; and the root biomass in this layer was 43% higher in VPs compared to BPs. The root biomass was significantly negatively correlated with bulk density (Table 2). As a result, the bulk density in the 0–10 cm, 10–20 cm, and 20–40 cm soil layers was 17%, 18%, and 16%, respectively, lower in VPs compared to BPs. The soil K_s was significantly different only in surface soil (0–10 cm), where the K_s was 124% higher in BPs than VPs (Table 1). The SOC in the 0–20 cm soil was higher in VPs than BPs. The SOC positively correlated with the root biomass (0.705**), clay (0.617**) and silt

Table 2
Correlations coefficients between soil properties of both bald and vegetation patches. IGWC: initial gravimetric water content; RB: root biomass; BD: bulk density; NCP: noncapillary porosity; CP: capillary porosity; FC: field capacity; SWHC: saturated water-holding capacity; K_s: saturated hydraulic conductivity; and SOC: soil organic carbon.

	IGWC	RB	BD	NCP	CP	FC	SWHC	K_S	SOC	Clay	Silt	Sand
IGWC	1	0.657**	−0.820**	0.417*	0.704**	0.873**	0.813**	−0.831**	0.863**	0.631**	0.820**	−0.804**
RB		1	−0.703**	0.665**	0.575**	0.765**	0.701**	−0.677**	0.705**	0.444*	0.473*	−0.473*
BD			1	−0.499*	−0.879**	−0.895**	−0.982**	0.624**	−0.895**	−0.586**	−0.725**	0.715**
NCP				1	0.398	0.445*	0.508*	−0.390	0.465*	0.185	0.202	−0.201
CP					1	0.854**	0.943**	−0.503*	0.759**	0.531**	0.672**	−0.660**
FC						1	0.916**	−0.759**	0.874**	0.609**	0.751**	−0.740**
SWHC							1	−0.630**	0.890**	0.615**	0.751**	−0.741**
K_S								1	−0.700**	−0.640**	−0.720**	0.716**
SOC									1	0.617**	0.761**	−0.750**
CLAY										1	0.922**	−0.939**
SILT											1	−0.999**

* $P < 0.05$.
** $P < 0.01$.

fractions (0.761**), and negatively correlated with the sand fraction (0.750**) (Table 2). Likewise, the root biomass was also positively correlated with the clay (0.444*) and silt (0.473*) fractions, and was negatively correlated with the sand fraction (0.473*).

3.2. Dominant flow behavior

The distribution of gravimetric soil water content was different between soil layers and between BPs and VPs (Fig. 2 d-f). A lateral flow, a type of preferential flow arising at the interface between soil layers having different permeability, occurred first at the 20 cm surface layer of soil profile from VPs to BPs (Fig. 2). The lateral flow continued in the 20–30 cm subsoil with an opposite direction, and high water was stored at the upper 30 cm of VPs (Fig. 2 d-f). To clarify, the dark blue dye stained area was significantly higher in VPs than BPs, while the light blue and green areas showed no significant differences between VPs and BPs (Fig. 3 A). The soil water content ranged from 17% to 40% (average of 32%) in VPs, and from 16 to 37% (average of 30%) in BPs,

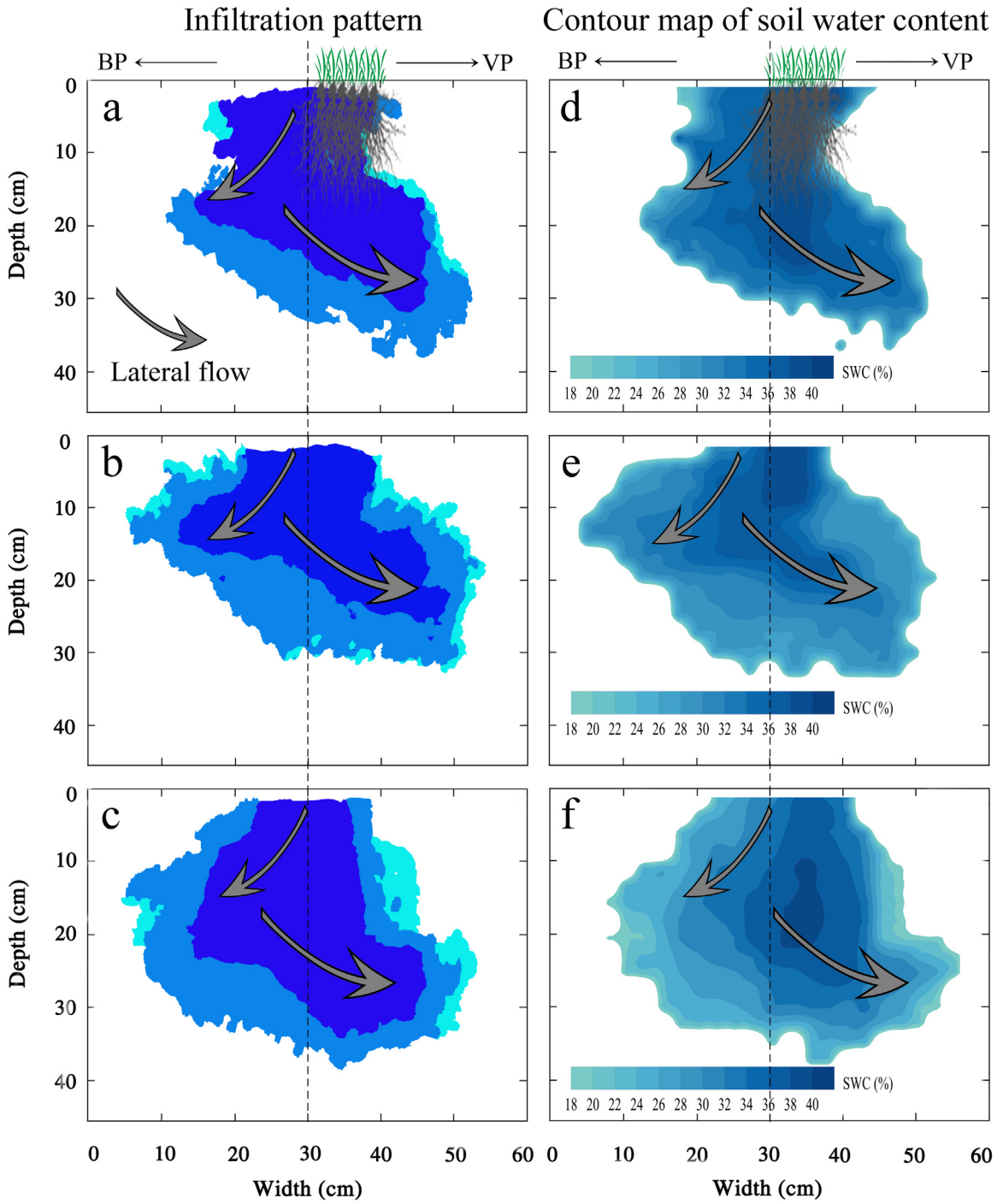

Fig. 2. Infiltration pattern (a, b, and c) and spatial distribution contour maps (d, e, and f) of soil water content (SWC) in the vertical profiles of interface between bald patches (BPs) and vegetation patches (VPs). The dark blue area indicates the flow paths that are heavily stained with Brilliant Blue FCF dye (>2.0 g L^{-1}) as water infiltrated the subsoil. The light blue and green areas are slightly stained with Brilliant Blue FCF dye, and the concentrations ranged from 0.5 to 2.0 g L^{-1} and from 0.05 to 0.5 g L^{-1}, respectively. The dark blue areas indicate preferential flow. The light blue and green areas indicate strong and weak interactions, respectively, between the macropores and the surrounding soil matrix. The kriging maps of the soil water content in the vertical soil profiles were produced through ordinary kriging with the Surfer program (Version 10.0, Golden Software Inc., Golden, CO, USA) after the gravimetric moisture content was measured.

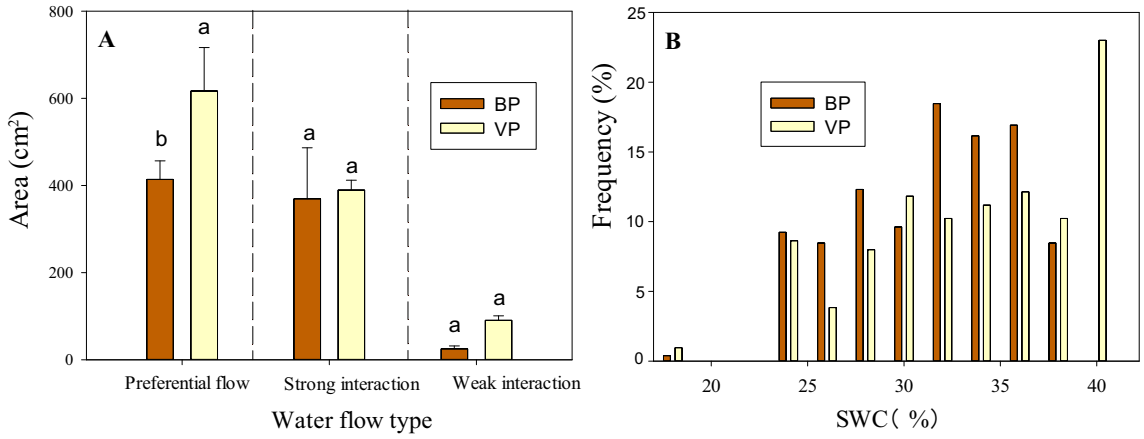

Fig. 3. Mean real area of the three water flow types (A) and frequency of soil water content (B) (SWC). The graphs present summarized data from the infiltration patterns and spatial distribution contour maps in the vertical profiles of interface between bald patches (BPs) and vegetation patches (VPs). Different letters within the same water flow type indicates a significant difference at 0.05 threshold.

though the modal value of water content was 27% higher in VPs than the BPs (Fig. 3 B). The estimated total stored water was lower in BPs than the VPs due to the larger stained area in VPs (Fig. 2 a-c). The subsoil water flowed uniformly in domain without BPs (Fig. 4m) compared to domains with interspersed BPs (Fig. 4 n-q); and for these latter the wetted area mainly restrained at the top soil of VPs. However, a wider area of interspersed BPs in the VPs induced a larger lateral flow in the domain subsoil (Fig. 4 n-q). As a result, the cumulative infiltration and bulk volume (1 cm × 1 cm × 1 cm) in BPs were linked by a simple linear relationship with coefficients of determination of 0.969 (Fig. 5).

3.3. Sediment yield

The sediment yield was lower in VPs than the BPs in 0–10 cm, 10–20 cm, 20–40 cm soil layers, while no difference in sediment yield occurred in the 40–60 cm layer (Fig. 6). The sediment yield in 0–10 cm and 10–20 cm layers was respectively 3.4-fold and 3.1-fold higher in BPs than the VPs during the first 5 min of artificial rainfall (Fig. 6). The redundancy analysis of the sediment yield and soil properties shows that the first two axes explained 91.1% of the total variance of soil variables (Fig. 7). The first ordination axis was mainly related to the sediment yield and SOC (Fig. 7). The correlations of sediment yield and soil properties with the first and second axes were 0.957 and 0.699, respectively. The sediment yields negatively correlated with soil properties such as noncapillary porosity, root biomass, clay, silt, initial water content, capillary porosity, saturated water-holding capacity, and field capacity, while it positively correlated with bulk density, sand, and K_s. SOC showed opposite relationships with these soil properties compared with sediment yield.

4. Discussion

4.1. Soil properties as affected by bald patches

Bald patches did not affect the soil properties in the deep soil layer of 20–60 cm (Table 1). However, the difference in soil properties between BPs and VPs was mainly observed at the surface 0–20 cm layer of the soil profile, because of the highest root biomass in this layer (Table 1). The root biomass of alpine meadow principally confined at the upper 20 cm of the soil profile, and the corresponding fluctuations in the soil physical properties mostly appeared in this layer (Table 1). The presence of root biomass in subsoil can involve two essential changes to

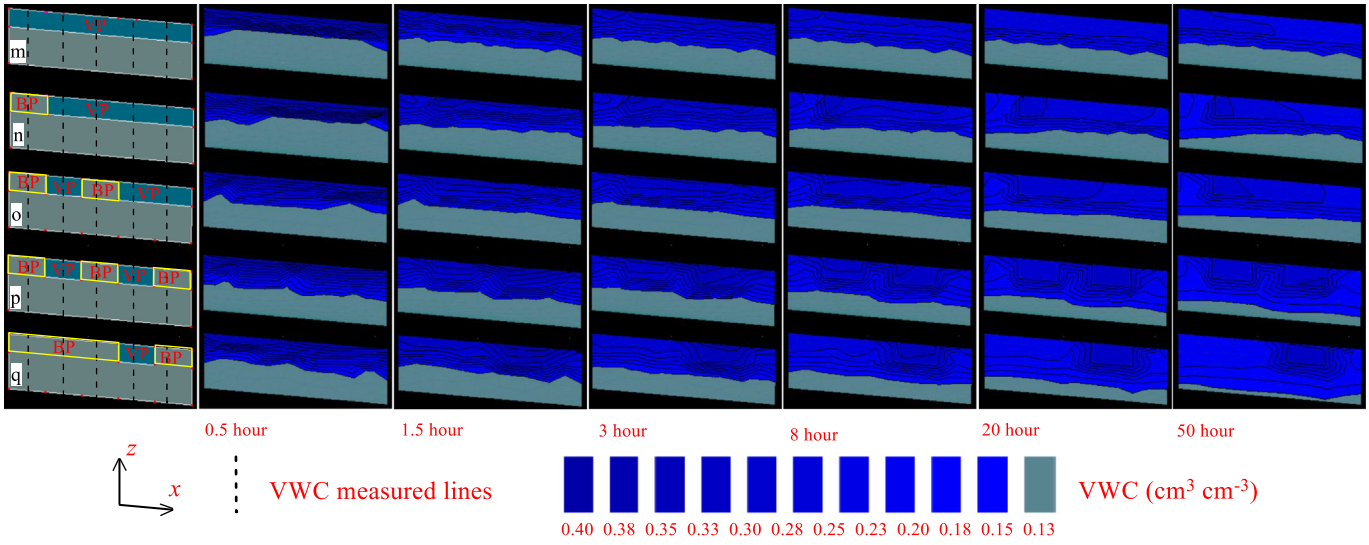

Fig. 4. Lateral flow was more dominant along with the greater BPs, which was simulated with HYDRUS-2/3D. Given that the significantly defference of K_s was observed in the top soil, we considered BP and VP (matched soil properties in soil depth of 0–10 cm in Table 1) as two material in this model. Rainfall intensity was 12 cm hour^{-1}. Various BPs/VPs configurations (m, 100% VPs; n, 80% VPs and 20% BPs; o, 60% VPs and 40% BPs; p, 40% VPs and 60% BPs; q, 20% VPs and 80% BPs).

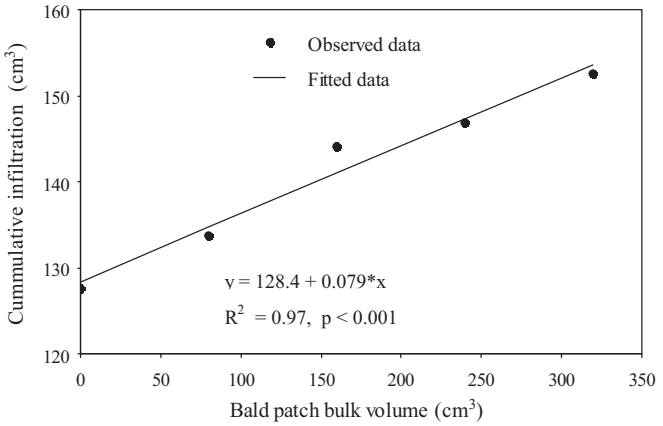

Fig. 5. Cumulative infiltration increased along with bald patch bulk volume. Cumulative infiltration (cm^3) = average VWC ($cm^3\ cm^{-3}$) × wetted area (cm^2) × soil thickness (cm). Bald patch bulk volume (cm^3) = vertical surface area (cm^2) × soil thickness (cm). Soil thickness was 1 cm.

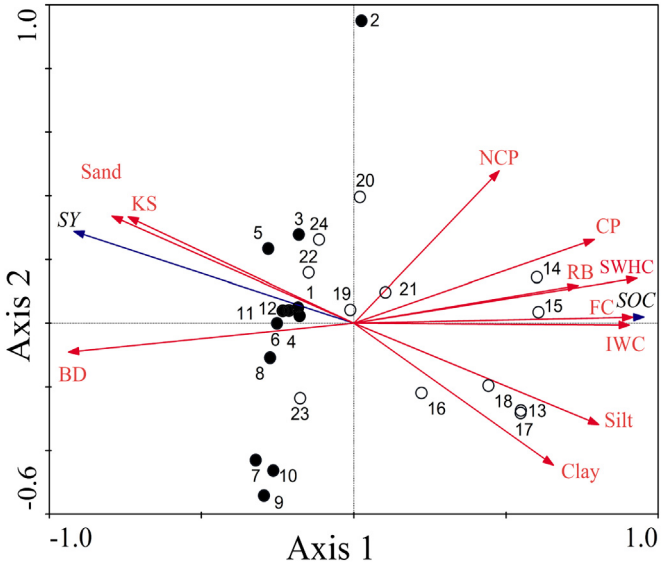

Fig. 7. Redundancy analysis ordination diagram of sediment yield (SY), soil organic content (SOC) and soil properties (SP). White dots indicate vegetation patches samples and black dots are bald patches samples. Soil properties refer to IWC: initial water content; BD: bulk density; NCP: non-capillary porosity; CP: capillary porosity; FC: field capacity; SWHC: saturated water-holding capacity; RB: root biomass; K_s: saturated hydraulic conductivity; silt, sand, and clay. The average value of three soil samples from the same soil layer was used as one point data for the redundancy analysis.

soil properties: (1) the roots activities (growth, development, and death) and root channels can directly affect soil bulk density, porosity, and K_s (Ilstedt et al., 2007; Benegas et al., 2014; Jiang et al., 2018), and (2) decayed roots can serve as a source of SOC (Carsan et al., 2014; Chen et al., 2018). Previous research found that bulk density, water-holding capacity, and SOC are primary indicators of grassland or meadow degradation (Dong et al., 2012). Here, the soil properties significantly varied between VPs and BPs, and between soil layers, apart from noncapillary porosity which did not vary among soil layers (Table 1).

The results from this study also show that the SOC was lower in BPs than the VPs, and this low SOC in BPs conducted to low porosity, field capacity, and saturated water-holding capacity, but high bulk density and K_s (Table 2, Fig. 7). This finding is consistent with previous findings where high SOC loss from soil results in high bulk density and low porosity; reducing the soil infiltration, water storage, and air storage capacity (Franzluebbers, 2002; Wall and Heiskanen, 2003; Celik, 2005). Moreover, Gregorich et al. (1994) reported that SOC is important in maintaining soil tilth, aiding infiltration and promoting agroecosystems water retention. However, for Piccolo and Mbagwu (1999) the degradation of soil properties is associated to a decrease in soil SOC hydrophilic components (e.g., polysaccharides), which may limit the surface soil water absorption. In this study, the SOC was lower in BPs than the VPs indicating both the decrease in SOC and deterioration of the other soil properties can be the consequences of the occurred BPs in QTP alpine meadow. The existence of BPs in QTP alpine meadow degrades its soil properties, and the degrading VPs can lead to severe environmental issues at the regional and global scales. This phenomenon is similar to the effect of unsustainable management practices (ploughing, overgrazing, and plant cover change) in alpine pasturelands (Li et al., 2007).

4.2. Water infiltration behavior as affected by bald patches

The degradation of alpine meadow has been of concern in the past years because of the importance and uniqueness of QTP eco-hydrology, the contribution of soil hydraulic properties and its associated internal factors (Li et al., 2007; Wang et al., 2007; Cheng et al., 2008). The increase in alpine meadow degradation has significantly reduced the root activity and SOC (Zeng et al., 2013), but raised the sand fraction (Table 1). These changes lead to high soil bulk density and low porosity, especially in BPs, thereby lowering the air and water storage capacities (Wall and Heiskanen, 2003; Celik, 2005), and disturbing the subsoil water flow behavior (Kabir et al., 2020). In this research, we used K_s, which represents the ability of soil to facilitate the water flux under

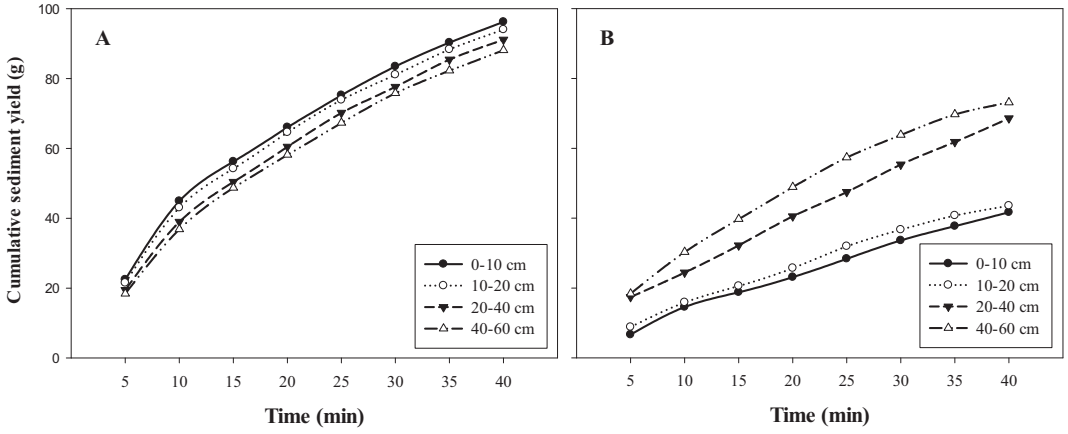

Fig. 6. Differences of cumulative sediment yield between various soil layers of the two patches. A, bald patches; B, vegetation patches.

saturated conditions (Kutílek, 2004), to analyze the soil water conductivity. Moreover, the volumetric water contents and HYDRUS-2/3D simulations were used to examine the dominant water flow at the interface between BPs and VPs.

The results of this study show that K_s was lower in VPs than the BPs for the top 0–20 cm layer (Table 1). This finding is in agreement with the results of Cheng (2008) and Zeng et al. (2013), but in conflict with the result of Wang et al. (2007) who found that soil K_s increases with the increasing vegetation degradation. This discrepancy can be due to the existing mattic epipedon layer which in our study site comparatively to that of Wang et al. (2007). The K_s of BPs soils significantly increased with the decreasing area of the mattic epipedon layer. This result was different from those in arid and semiarid zones where the K_s is higher in VPs than the BPs (Assouline et al., 2015) or increases along with aboveground biomass of VPs (Thompson et al., 2010). Besides, the K_s of both BPs and VPs significantly correlated with bulk density, porosity, soil organic matter, and root density, which was consistent with the conclusions of Zeng et al. (2013). However, as expected the K_s negatively linked to root biomass (-0.677, $P < 0.01$, Table 2) because of the high entwined roots at the topsoil soil layers (mainly in VPs) of the mattic epipedon layer that can reduce the water permeability.

In the system BPs-VPs, VPs with low K_s generated high runoff during rainfall, and BPs with high K_s accepted and infiltrated the produced runoff. Therefore, the presence of BPs in the QTP can amplify the effect of spatial variation of water infiltration and runoff on the water distribution in soil of alpine meadow. This result was different from previous findings where BPs are the sources of runoff water, sediments, nutrients and other soil materials (Carmi and Berliner, 2008; Kakembo, 2009; Davis et al., 2010); while VPs are sinks of these materials (Eldridge and Greene, 1994; Boer and Puidefábregas, 2005; Itzhak et al., 2007). Thus, BPs play a major role in the distribution of water, nutrients, and sediment (Carmi and Berliner, 2008; Kakembo, 2009; Davis et al., 2010). Such differences in soil properties between BPs and VPs can also affect the distribution pattern of vegetation cover (Wamelink et al., 2018).

The existence of BPs in the VPs highly affected the QTP subsoil water flow behavior. The subsoil water flowed uniformly in domains without BPs (Fig. 4 m) compared to the domains with interspersed BPs (Fig. 4 n-q). Thus, a lateral flow occurred, both at point and slope scales, from VPs to BPs in the top soil layer (0–20 cm); then, it expanded wider from the shallow layer of BPs to the deep soil layer of VPs in the subsoil (> 20 cm) (Figs. 2 and 4). Wider was the area of BPs in the VPs, larger was the lateral flow in the subsoil (Fig. 4 n-q), resulting in a linear relationship between cumulative infiltration and BPs bulk volume ($R^2 = 0.969$, Fig. 5). The lateral flow became more dominant in the subsurface than in shallow soil, along with the increasing area of BPs, leading to more water infiltration into soil (Figs. 4 and 5). The roots at the soil surface have potential to retain soil moisture (Wang et al., 2007; Cheng et al., 2008), resulting in higher soil moisture in VPs than the BPs and in 20–50 cm subsoil than the 0–10 cm layer (Table 1 and Fig. 2). In short, the presence of BPs in the QTP created a heterogeneity of its soil physical and biological properties, which can change the soil K_s and water storage capacity, as well as the water flow patterns and water flow behavior in the system BPs-VPs.

4.3. Sediment yield as affected by bald patches

The existence of BPs in the QTP affected its soil erosion. The sediment yield was negatively correlated with the root biomass, SOC, clay, and silt fractions; while it was positively correlated with bulk density, sand fraction and K_s (Table 2 and Fig. 7). The high bulk density and sand provided original materials for the sediment yield, and water flow with high K_s could carry the lost sediment. Previous research found that SOC can adhere to soil particles to reduce sediment loss (Gregorich et al., 1994; Kay, 2000). Once BPs occurs on the QTP, this latter lose its soil cover and the water erosion reduces SOC and other nutrients from soil (Su et al., 2006; Mekuria et al., 2012; Wang et al., 2014). Water erodes 14.1 t ha^{-1} of sediment and 0.69 t ha^{-1} of SOC annually, leading to a loss of small soil particles and an increase in the fraction of larger soil particles (Su et al., 2006; Al-Farraj, 2008; Hu et al., 2016). The SOC significantly and positively correlated with clay and silt fractions, but negatively correlated with the sand fraction (Table 2). As a result, particles such as clay and silt were washed away by runoff during the formation of BPs, leading to the emergence of coarse texture at the upper soil layer (Table 1).

About one quarter of the total sediment eroded in the first 5 min of the artificial rainfall. The sediment yield was 37% higher in the BPs than the VPs. Moreover, for the first 5 min of simulated rain, sediment yield of VPs was 131% lower in the shallow 0–20 cm layer (with root) than in the deep 20–40 cm (without root) layer, while BPs experienced opposite trend with 14% higher sediment yield in shallow layer than the deep layer (Fig. 6). Such difference of sediment yield between VPs and BPs can be mainly due to the root system of the alpine meadow, which was confined in the upper 20 cm of the soil profile (Table 1). This difference in sediment yield between VPs and BPs could become heavier along with the increasing slope (Bouchnak et al., 2009). Previous research reported that more than half of the roots of alpine meadow spreads in the 0–20 cm depth (Yan et al., 2001; Wang et al., 2009; Zeng et al., 2013). The cumulative sediment yield was higher in the BPs than the VPs (Fig. 6), suggesting a potential contribution of each soil layer on soil erosion once the cover of alpine meadow disappears. The sediment yields were negatively correlated with the root biomass (-0.578, $P < 0.01$), and clay (-0.754, $P < 0.01$), and silt (-0.855, $P < 0.01$) fractions; while it was positively correlated with sand fraction (0.850, $P < 0.01$) and K_S (0.71, $P < 0.01$) (Table 2 and Fig. 7). The adhesion of root system to soil can serve as an important physical barrier, protecting the soil particles both from subsurface water flow and runoff erosions (lateral flow and overland flow), and the mattic epipedon layer on soil surface can directly reduce rain splash erosion.

4.4. Process of alpine meadow degradation

The formation of BPs, leading to alpine meadow degradation, was mediated by the roots loss in the 0–20 cm soil layer, followed by sediment erosion which principally depended on the interrelationship between soil properties. BPs took place after loss of the VPs vegetation cover and high sediment loss, which lowers the ground surface of alpine meadow and progressively increased the size of BPs (Fig. 8 A). As a result, the root system in the soil decreases and the soil particles settle at surface soil layer of BPs. This occurring soil fraction in BPs (without root system) was easily moved and eroded by high water flow (Fig. 8 B), leading to two common phenomena in Beiluhe basin: (1) a lateral flow occurred at subsurface layer (Fig. 8 C), and (2) some isolated VPs were easily eroded, removed, slid down, and lost (Fig. 8 D). Indeed, the simulated rainfall mainly eroded the smallest soil particles from the BPs to form a coarse surface soil layers, and the downcutting of headwards erosion lowered its ground levels. The created lower ground level of BPs relative to the ground level of VPs alternated to form an erosion interface, where raindrops detached soil particles which was likely eroded by lateral flows. Raindrops also easily separated or stripped the marginal alpine meadows (especially, those near the lower edge of VPs), then washed them away through runoff (Figs. 6 and 8).

The processes and compositions of runoff in the QTP are mainly controlled by bidirectional freezing of the active layer (Zhang et al., 2011; Wang et al., 2017). Here, we designed a conceptual model to understand the impact of freezing-thawing on soil erosion in unidirectional freezing over the ground (Fig. 9). Thus, considering the thickness of the active layer (only 140 cm) and the results from the above sections, (1) the soil freeze earlier in the lands with small vegetation coverage, then (2) the frost heave or upheaval becomes more substantial in areas with high water content (egg. VPs). Previous study suggested

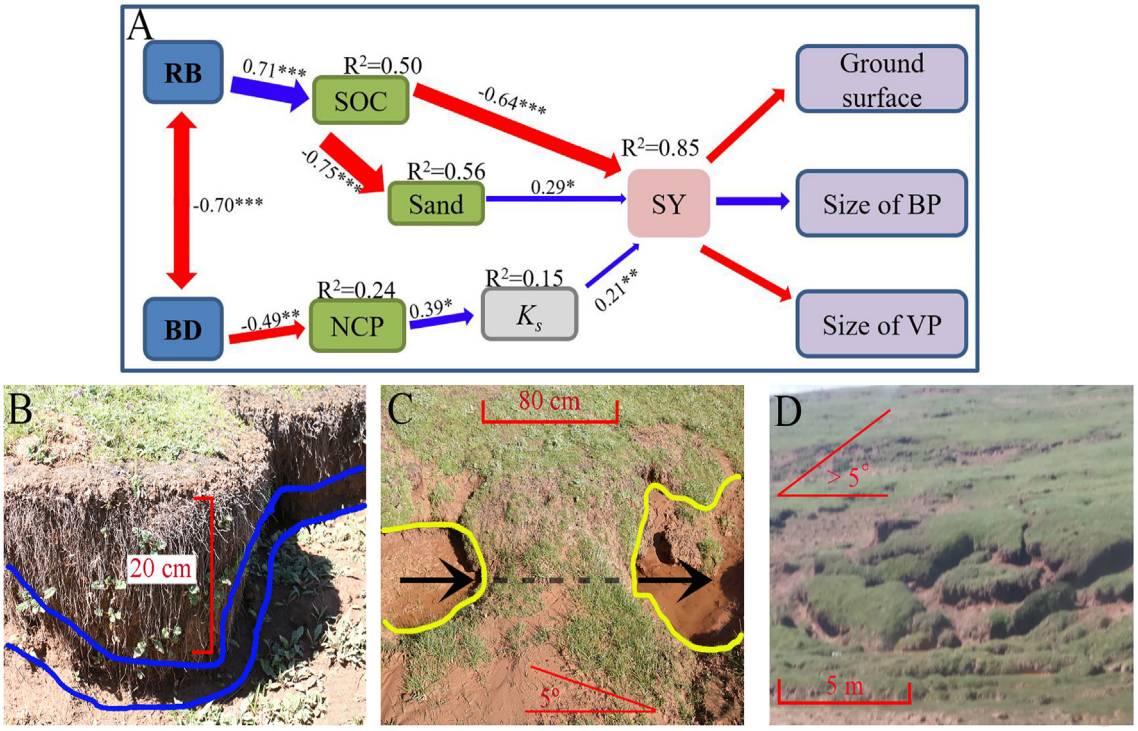

Fig. 8. Structural equation model (A) and field evidence (B, C, and D) demonstrate that plausible pathways through which K_s could enhance sediment yield (SY) and the indirect effects of RB and BD on SY. Arrow widths indicate the strength of standardized path coefficients. The numbers associated with the arrows indicate the path coefficients calculated from Mantel correlations. R^2 value represents the proportion of total variance explained for the specific dependent variable. $\chi^2 = 58.983$, df = 13, probability level = 0.000, RMSEA = 0.392, AIC = 102.983. B: Root biomass confined to the upper 20 cm of the soil profile. The belt area marked by blue line shows that the soil particles (without the adherence of root systems) easily eroded by lateral flow, rainfall, wind, and so on. C: A pipe flow appeared when soil particles eroded by lateral flow that occurred at the surface between BP and VP. D: some isolated VPs could be removed, slid down, and lost when soil particles between BPs and VPs eroded by lateral flow. Thus, various water flow behavior could provide different water content for the soil layers, inducing a disturbance in the freezing-thawing process between meadow soil layers. RB: root biomass; BD: bulk density; NCP: non-capillary porosity; SOC: soil organic content; K_s: saturated hydraulic conductivity.

that the beginning of freezing is linked to vegetation coverage (Wu et al., 2003). The size of the frost heave was affected by soil water content and can in turn influence the soil K_s and soil water flow behavior (Fig. 9 B). The soil with higher water content can release and absorb more heat during the freezing-thawing process (Wang et al., 2007; Cheng et al., 2008).

The difference in soil water content between BPs and VPs affected soil freezing times in the system BPs-VPs, resulting in frost heaves in the gentle slope surface soil between two adjacent BPs and VPs (Fig. 9 C). These slope patches may block heat dissipation from VPs subsoil during winter, and serve as heat insulation and temperature buffer (Wu et al., 2003). Thus, the thawing process in VPs was lagged behind that in the BPs at the soil interface, resulting in the formation of thaw slump at the soil interface between VPs and BPs (Fig. 9 D). Previous research similarly found that small freeze-thawing solifluctions creep occurs mainly in the shallow surface (Harris and Davies, 2000; Matsumoto et al., 2010). Consequently, the soil can be moved across the active soil layer with water as a lubricant, because of the difference in K_s between the soil layers of BPs and VPs. Wang et al. (2018) similarly reported that the ground above the sliding surface is easily deformed and displaced after undergoing a year-round cycle of freezing and thawing. To conclude, soil water content can obviously affect freezing-thawing process of the active permafrost layer and solifluctions creep process, which in turn may accelerate the degradation of alpine meadow in Beiluhe basin. The degradation will become more serious when more water infiltrates into the soil along with the increasing area of the BPs (Figs. 4 and 5). Thus, BPs can spread very fast after experiencing several degradation processes (Fig. 9), increasing the desertification process in the QTP with the formation of sparse small–sized thermokarst lakes.

The current study improves our understanding of the degradation of alpine meadow soil and its ecosystem. It also enables us to predict the changes in QTP to provide guidelines that can help to improve the water flow modelling in QTP and similar regions. Considering the wide distribution of BPs on the QTP in China, and the difficulty to totally restore the QTP (Wang et al., 2007), the degradation of alpine meadows can be controlled through the guidance of relevant principles: a cover of residues (crop, vegetation, plastic mulch, etc.) should be maintained on bald soil surface once soil vegetation is removed to delay the formation of BPs. This strategy can reduce the special variation of soil water content and soil properties in the QTPs, and weaken the freezing-thawing and erosions which lead to the formation of BPs.

Many areas of the world share similar features with our study site. Thus, the findings from this research are not only restricted to alpine meadow of QTP. Our results are also applicable to alpine tundra ecosystem in Changbai Mountain (Northeast China), and even other ecosystems such as alpine vegetation in Japan; alpine tundra ecosystem in North American (USA, Canada) and South American (Peru) (Schorghofer et al., 2017); alpine ecosystems in the Pacific Islands (Hawai'i, New Zealand, and New Guinea) or in Africa Tropical Mountains (Kenya, Tanzania, Mt. Kilimanjaro, and Uganda); and permafrost zones in Europe (Abramov et al., 2008; Vieira et al., 2010) and Antarctica. Since surface vegetation is very sensitive to temperature (Solangi et al., 2019), and the alpine meadow/tundra supplies water for many downstream uses; it will be interesting to know how water resources could affect the future changes in precipitation, evapotranspiration, and the accumulation and loss of snowpack in high mountains and cold regions.

5. Conclusions

The incidence of BPs in QTP widely affected the degradation of alpine meadows. This study used a combination of methods (soil properties,

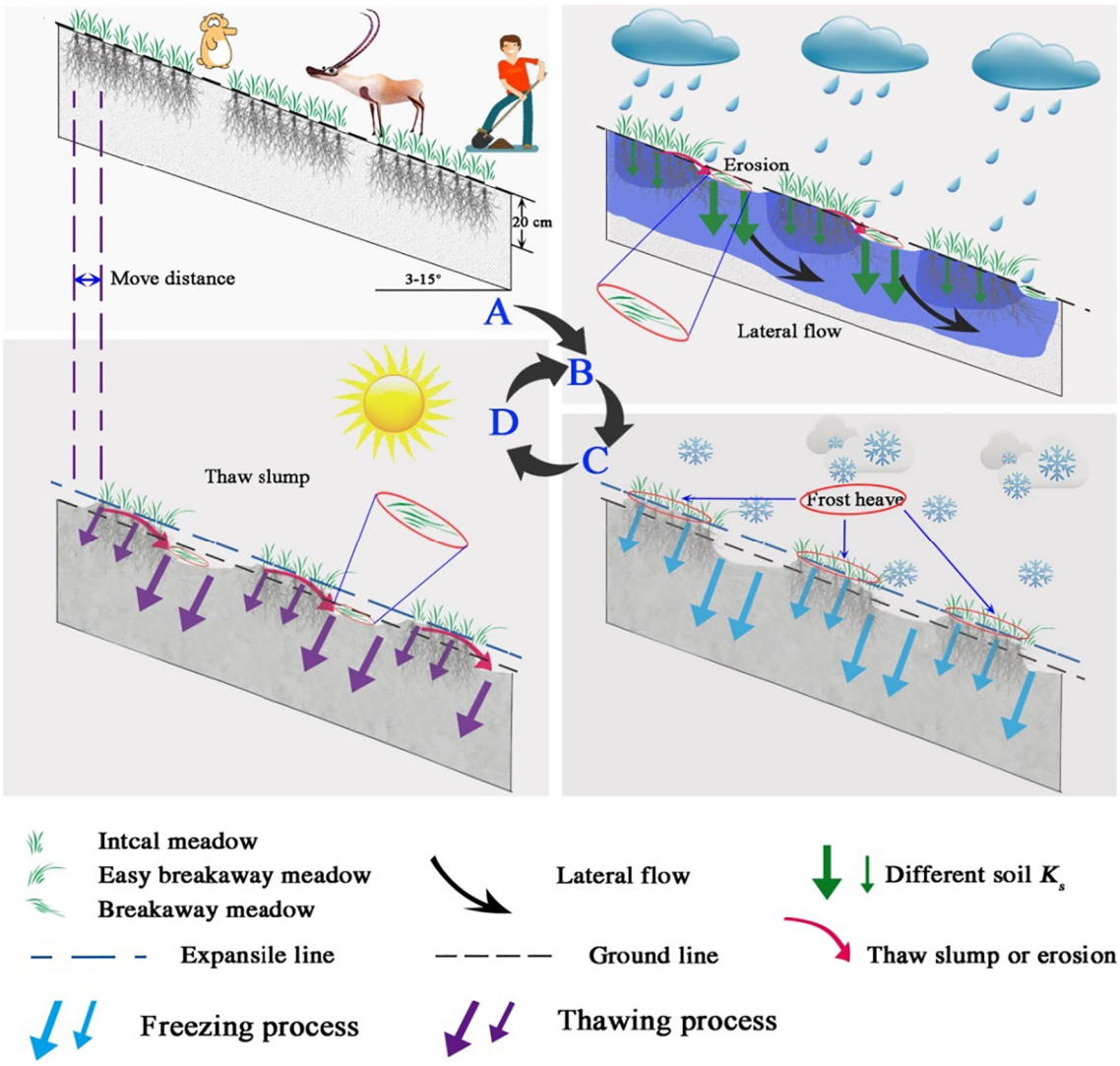

Fig. 9. Conceptual diagram of the underlying mechanisms controlling the alpine meadow degradation in the Qinghai-Tibetan Plateau of China. A: bald patches resulting from overgrazing, human and plateau pika (*Ochotona curzoniae*) activities. B: Marginal meadow and soil particles eroded readily by rainfall and lateral flow. C: Frost heave in the surface soil resulting from different episodes of soil freezing and variation of soil water flow behavior between vegetation patches and bald patches. D: Thaw slump at the soil interface between vegetation patches and bald patches resulting from the differences in thawing processes at this soil interface. Move distance shows the degradation of the vegetation patches after a cycle of the mechanisms (A to D); where vegetation patches area was reduced expanding the area of bald patches.

soil erodibility, and water infiltration patterns) to interpret the impact of BPs on the underlying mechanisms of QTP soil water storage and associated soil erosion, which substantially contributed to the degradation of alpine meadow. Both the mattic epipedon layer and over half of the entwined roots system on the top soil (0–20 cm) of VPs contribute to the difference in soil properties between BPs and VPs. In addition, about one quarter of the total sediment eroded in the first 5 min of the artificial rainfall, and the sediment yield was 37% higher in the BPs than the VPs. Based on these findings, the BPs soils erode faster than those of the VPs; and the downcutting of headward erosion lowers the ground levels of BPs. The created lower ground level of BPs relative to the ground level of VPs alternated to form an erosion interface, where marginal meadow is likely detached by raindrops, and washed away through runoff. Concomitantly, the mattic epipedon layer in the VPs directly reduced the impact of raindrops, and the adhesion of its root system prevents soil particles from stripping and washing away by runoff. The saturated hydraulic conductivity (K_s) at the surface soil (0–10 cm) was 124% higher in BPs than the VPs. Therefore, the strewing of BPs in the VPs caused a spatial variation of infiltration and runoff in QTP, leading to higher infiltration capacity of the BPs soils compared to those of VPs. This difference in K_s between the two patches conducted to soil layers with different water contents; and a lateral flow occurred from BPs to VPs. Such soil and water feature can disturb both the freezing-thawing process and the thaw slump rate between soil layers; accelerating the alpine meadow degradation. The degradation would become more serious if BPs continued to propagate in the QTP. This research highlight that the differences in soil physical and hydrological properties between BPs and VPs would provoke the alpine meadow degradation in the QTP. Future study would focus on the relationship between vegetation recovery and alpine meadow degradation in other high desert and cold systems. A limitation of this study is the use of higher rainfall intensity for the simulated erosion experiments compared to the maximum rain intensity of our study sites. Such higher rain intensity might overestimate the amount of eroded soil particles compared to the real environment. However, it will not affect the comparison of soil loss between soil layers and between BPs and VPs.

CRediT authorship contribution statement

Xiao-Jin Jiang: Conceptualization, Funding acquisition, Methodology, Investigation, Formal analysis, Visualization, Writing - original draft, Writing - review & editing. **Xiai Zhu:** Formal analysis. **Zi-Qiang Yuan:**

Investigation, Writing - review & editing. **Xiao Gang Li:** Writing - review & editing. **Wenjie Liu:** Project administration, Funding acquisition, Supervision. **Sissou Zakari:** Formal analysis, Writing - review & editing, Supervision.

Declaration of competing interest

The authors declare that they have no known competing financial interests or personal relationships that could have appeared to influence the work reported in this paper.

Acknowledgments

We thank Mr. Liu MN for his help in the fields. We also thank the Central Laboratory of XTBG for their help. This research was supported by the National Natural Science Foundation of China (41701029 and 31570622), the Youth Innovation Promotion Association CAS (2018430), the Natural Science Excellent Youth Foundation of Yunnan Province (2019FI011), the Yunnan Fundamental Research Projects (grant NO. 2018FB076, 2014HB042), and the CAS 135-Program (No. 2017XTBG-F01).

References

Abramov, A., Gruber, S., Gilichinsky, D., 2008. Mountain permafrost on active volcanoes: field data and statistical mapping, Klyuchevskaya volcano group, Kamchatka, Russia. Permafrost periglac 19, 261–277. https://doi.org/10.1002/ppp.622.

Al-Farraj, A., 2008. Desert pavement development on the lake shorelines of Lake Eyre (south), South Australia. Geomorphology 100 (1–2), 154–163. https://doi.org/10.1016/j.geomorph.2007.10.029.

Assouline, S., Thompson, S.E., Chen, L., Svoray, T., Sela, S., Katul, G.G., 2015. The dual role of soil crusts in desertification. J. Geophys. Res-Biogeo. 120 (10), 2108–2119. https://doi.org/10.1002/2015JG003185.

Barberá, G.G., Navarro-Cano, J.A., Castillo, V., 2007. Vegetation pattern and land degradation. In: Hooke, J. (Ed.), Conditions for Restoration and Mitigation of Desertified Areas Using Vegetation (RECONDES). European Community, Luxembourg, pp. 97–100.

Barger, N.N., Herrick, J.E., Zee, J.V., Belnap, J., 2006. Impacts of biological soil crust disturbance and composition on C and N loss from water erosion. Biogeochemistry 77 (2), 247–263. https://doi.org/10.1007/s10533-005-1424-7.

Belnap, J., 2006. The potential roles of biological soil crusts in dryland hydrologic cycles. Hydrol. Process. 20 (15), 3159–3178. https://doi.org/10.1002/hyp.6325.

Benegas, L., Ilstedt, U., Roupsard, O., Jones, J., Malmer, A., 2014. Effects of trees on infiltrability and preferential flow in two contrasting agroecosystems in Central America. Agric. Ecosyst. Environ. 183, 185–196. https://doi.org/10.1016/j.agee.2013.10.027.

Bodhinayake, W., Si, B.C., Noborio, K., 2005. Determination of hydraulic properties in sloping landscapes from tension and double-ring infiltrometers. Vadose Zone J. 3 (3), 964–970. https://doi.org/10.2113/3.3.964.

Boer, M., Puidefábregas, J., 2005. Effects of spatially structured vegetation patterns on hillslope erosion in a semiarid Mediterranean environment: a simulation study. Earth Surf. Process. Landf. 30 (2), 149–167. https://doi.org/10.1002/esp.1180.

Bouchnak, H., Felfoul, M.S., Boussema, M.R., Snane, M.H., 2009. Slope and rainfall effects on the volume of sediment yield by gully erosion in the Souar lithologic formation (Tunisia). Catena 78 (2), 170–177. https://doi.org/10.1016/j.catena.2009.04.003.

ter Braak, C.J.F., Smilauer, P., 2002. CANOCO Reference Manual and User's Guide to Canoco for Windows: Software for Canonical Community Ordination (Version 4.5). Micro-Computer Power, Ithaca, NY, US.

Carmi, G., Berliner, P., 2008. The effect of soil crust on the generation of runoff on small plots in an arid environment. Catena 74 (1), 37–42. https://doi.org/10.1016/j.catena.2008.02.002.

Carsan, S., Stroebel, A., Dawson, I., Kindt, R., Mbow, C., Mowo, J., Jamnadass, R., 2014. Can agroforestry option values improve the functioning of drivers of agricultural intensification in Africa? Curr. Opin. Environ. Sustain. 6, 35–40. https://doi.org/10.1016/j.cosust.2013.10.007.

Celia, M.A., Bouloutas, E.T., Zarba, R.L., 1990. A general mass-conservative numerical solution for the unsaturated flow equation. Water Resour. Res. 26 (7), 1483–1496. https://doi.org/10.1029/WR026i007p01483.

Celik, I., 2005. Land-use effects on organic matter and physical properties of soil in a southern Mediterranean highland of Turkey. Soil Tillage Res. 83 (2), 270–277. https://doi.org/10.1016/j.still.2004.08.001.

Cey, E.E., Rudolph, D.L., 2009. Field study of macropore flow processes using tension infiltration of a dye tracer in partially saturated soils. Hydrol. Process. 23 (12), 1768–1779. https://doi.org/10.1002/hyp.7302.

Chen, J., Yi, S., Qin, Y., 2017. The contribution of plateau pika disturbance and erosion on patchy alpine grassland soil on the Qinghai-tibetan plateau: implications for grassland restoration. Geoderma 297, 1–9. https://doi.org/10.1016/j.geoderma.2017.03.001.

Chen, C.F., Liu, W.J., Wu, J.N., Jiang, X.J., 2018. Spatio-temporal variations of carbon and nitrogen in biogenic structures of two fungus-growing termites (*M. annandalei* and *O. yunnanensis*) in the Xishuangbanna region. Soil Biol. Biochem. 117, 125–134. https://doi.org/10.1016/j.soilbio.2017.11.018.

Cheng, Y.T., 2008. The Study in the Infiltration Process and the Factors of the Soil Moisture in the Permafrost Alpine Meadow. Lanzhou University, Gansu, Lanzhou, pp. 34–36.

Cheng, G., Jin, H., 2013. Permafrost and groundwater on the Qinghai-Tibet Plateau and in northeast China. Hydrogeol. J. 21 (1), 5–23. https://doi.org/10.1007/s10040-012-0927-2.

Cheng, H., Wang, G., Hu, H., Wang, Y., 2008. The variation of soil temperature and water content of seasonal frozen soil with different vegetation coverage in the headwater region of the Yellow River, China. Environ. Geol. 54 (8), 1755–1762. https://doi.org/10.1007/s00254-007-0953-x.

Danielson, R.E., Sutherland, P.L., 1986. Porosity. Methods of Soil Analysis: Part 1-Physical and Mineralogical Methods. methodsofsoilan1, pp. 443–461.

Davis, W.L., Pater de, I., McKay, C.P., 2010. Rain infiltration and crust formation in the extreme arid zone of the Atacama Desert, Chile. Planet. Space Sci. 58 (4), 616–622. https://doi.org/10.1016/j.pss.2009.08.011.

Dong, S.K., Wen, L., Li, Y.Y., Wang, X.X., Zhu, L., Li, X.Y., 2012. Soil-quality effects of grassland degradation and restoration on the Qinghai-Tibetan Plateau. Soil Sci. Soc. Am. J. 76 (6), 2256–2264. https://doi.org/10.2136/sssaj2012.0092.

Eldridge, D.J., Greene, R.S.B., 1994. Microbiotic soil crusts: a review of their role in soil and ecological processes in the rangeland of Australia. Aust. J. Soil Res. 32 (3), 389–415. https://doi.org/10.1071/sr9940389.

Flury, M., Flühler, H., 1995. Tracer characteristics of brilliant blue FCF. Soil Sci. Soc. Am. J. 59 (1), 22–27. https://doi.org/10.2136/sssaj1995.03615995005900010003x.

Forrer, I., Papritz, A., Kasteel, R., Flühler, H., Luca, D., 2000. Quantifying dye tracers in soil profiles by image processing. Eur. J. Soil Sci. 51 (2), 313–322. https://doi.org/10.1046/j.1365-2389.2000.00315.x.

Franzluebbers, A.J., 2002. Water infiltration and soil structure related to organic matter and its stratification with depth. Soil Tillage Res. 66 (2), 197–205. https://doi.org/10.1016/S0167-1987(02)00027-2.

van Genuchten, M.T., 1980. A closed-form equation for predicting the hydraulic conductivity of unsaturated soils. Soil Sci. Soc. Am. J. 44 (5), 892–898. https://doi.org/10.2136/sssaj1980.03615995004400050002x.

Gregorich, E.G., Carter, M.R., Angers, D.A., Monreal, C.M., Ellert, B.H., 1994. Towards a minimum data set to assess soil organic matter quality in agricultural soils. Can. J. Soil Sci. 74 (4), 367–385. https://doi.org/10.4141/cjss94-051.

Grenier, C., Régnier, D., Mouche, E., Benabderrahmane, H., Costard, F., Davy, P., 2013. Impact of permafrost development on groundwater flow patterns: a numerical study considering freezing cycles on a two-dimensional vertical cut through a generic river-plain system. Hydrogeol. J. 21 (1), 257–270. https://doi.org/10.1007/s10040-012-0909-4.

Guebert, M.D., Gardner, T.W., 2001. Macropore flow on a reclaimed surface mine: infiltration and hillslope hydrology. Geomorphology 39 (3–4), 151–169. https://doi.org/10.1016/s0169-555x(00)00107-0.

Harris, R.B., 2010. Rangeland degradation on the Qinghai-Tibetan plateau: a review of the evidence of its magnitude and causes. J. Arid Environ. 74 (1), 1–12. https://doi.org/10.1080/15230430.2000.12003356.

Harris, C., Davies, M.C.R., 2000. Gelifluction: observations from large-scale laboratory simulations. Arct. Antarct. Alp. Res. 32 (2), 202–207. https://doi.org/10.2307/1552452.

Hu, G., Liu, H., Yin, Y., Song, Z., 2016. The role of legumes in plant community succession of degraded grassland in northern China. Land Degrad. Dev. 27 (2), 366–372. https://doi.org/10.1002/ldr.2382.

Ilstedt, U., Malmer, A., Elke, V., Murdiyarso, D., 2007. The effect of afforestation on water infiltration in the tropics: a systematic review and meta-analysis. For. Ecol. Manag. 251 (1–2), 45–51. https://doi.org/10.1016/j.foreco.2007.06.014.

Issa, O.M., Valentin, C., Rajot, J.L., Cerdan, O., Desprats, J.-F., Bouchet, T., 2011. Runoff generation fostered by physical and biological crusts in semi-arid sandy soils. Geoderma 167-168, 22–29. https://doi.org/10.1016/j.geoderma.2011.09.013.

Itzhak, K., Blumberg, D.G., Lavee, H., Sarah, P., 2007. Spatial distribution dynamics of topsoil moisture in shrub microenvironment after rain events in arid and semi-arid areas by means of high resolution maps. Geomorphology 86 (3–4), 455–464. https://doi.org/10.1016/j.geomorph.2006.09.020.

Jiang, X.J., Liu, X.E., Wang, E.H., Li, X.G., Sun, R., Shi, W.J., 2015. Effects of tillage pan on soil water distribution in alfalfa-corn crop rotation systems using a dye tracer and geostatistical methods. Soil Tillage Res. 150, 68–77. https://doi.org/10.1016/j.still.2015.01.009.

Jiang, X.J., Liu, W., Wang, E., Zhou, T., Xin, P., 2017. Residual plastic mulch fragments effects on soil physical properties and water flow behavior in the Minqin Oasis, northwestern China. Soil Tillage Res. 166, 100–107. https://doi.org/10.1016/j.still.2016.10.011.

Jiang, X.J., Liu, W.J., Chen, C.F., Liu, J.Q., Yuan, Z.Q., Jin, B.C., Yu, X.Y., 2018. Effects of three morphometric features of roots on soil water flow behavior in three sites in China. Geoderma 320, 161–171. https://doi.org/10.1016/j.geoderma.2018.01.035.

Kakembo, V., 2009. Vegetation patchiness and implications for landscape function: the case of Pteronia incana invader species in Ngqushwa rural municipality, eastern Cape, South Africa. Catena 77 (3), 180–186. https://doi.org/10.1016/j.catena.2008.12.014.

Kakembo, V., Ndlela, S., Cammeraat, E., 2012. Trends in vegetation patchiness loss and implications for landscape function: the case of Pteronia incana invasion in the eastern Cape Province, South Africa. Land Degrad. Dev. 23 (6), 548–556. https://doi.org/10.1002/ldr.2175.

Kay, B.D., 2000. Soil structure. In: Sumner, E.M. (Ed.), Handbook of Soil Science. CRC Press, Boca Raton London, New York, Washington, D.C, pp. A229–A264.

Kutílek, M., 2004. Soil hydraulic properties as related to soil structure. Soil Tillage Res. 79 (2), 175–184. https://doi.org/10.1016/j.still.2004.07.006.

Li, X.G., Li, F.M., Zed, R., Zhan, Z.Y., Bhupinderpal-Singh, 2007. Soil physical properties and their relations to organic carbon pools as affected by land use in an alpine pasture-land. Geoderma 139 (1), 98–105. https://doi.org/10.1016/j.geoderma.2007.01.006.

Li, X.J., Li, X.R., Song, W.M., Gao, Y.P., Zheng, J.G., Jia, R.L., 2008. Effects of crust and shrub patches on runoff, sedimentation, and related nutrient (C, N) redistribution in the

desertified steppe zone of the Tengger Desert, northern China. Geomorphology 96 (1–2), 221–232. https://doi.org/10.1016/j.geomorph.2007.08.006.

Matsumoto, H., Yamada, S., Hirakawa, K., 2010. Relationship between ground ice and solifluction: field measurements in the Daisetsu Mountains, northern Japan. Permafr. Periglac. Process. 21 (1), 78–89. https://doi.org/10.1002/ppp.675.

Mekuria, A., Vlek, P.L.G., Denich, M., 2012. Application of the caesium-137 technique to soil degradation studies in the southwestern highlands of Ethiopia. Land Degrad. Dev. 23 (5), 456–464. https://doi.org/10.1002/ldr.1088.

Meyer, L.D., Harmon, W.C., 1984. Susceptibility of agricultural soils to interrill erosion. Soil Sci. Soc. Am. J. 48 (5), 1152–1157. https://doi.org/10.2136/sssaj1984.03615995004800050040x.

Miller, B.A., Schaetzl, R.J., 2012. Precision of soil particle size analysis using laser diffractometry. Soil Sci. Soc. Am. J. 76 (5), 1719–1727. https://doi.org/10.2136/sssaj2011.0303.

Pan, X., Yu, Q., You, Y., Chun, K.P., Shi, X., Li, Y., 2017. Contribution of supra-permafrost discharge to thermokarst lake water balances on the northeastern Qinghai-Tibet plateau. J. Hydrol. 555, 621–630. https://doi.org/10.1016/j.jhydrol.2017.10.046.

Piccolo, A., Mbagwu, J.S.C., 1999. Role of hydrophobic components of soil organic matter in soil aggregate stability. Soil Sci. Soc. Am. J. 63, 1801–1810. https://doi.org/10.2136/sssaj1999.6361801x.

Schaap, M.G., Leij, F.J., van Genuchten, M.T., 2001. ROSETTA: a computer program for estimating soil hydraulic parameters with hierarchical pedotransfer functions. J. Hydrol. 251 (3–4), 163–176. https://doi.org/10.1016/S0022-1694(01)00466-8.

Schorghofer, N., Leopold, M., Yoshikawa, K., 2017. State of high-altitude permafrost on tropical Maunakea volcano, Hawaii. Permafrost periglac 28, 685–697. https://doi.org/10.1002/ppp.1954.

Šimůnek, J., Šejna, M., van Genuchten, M.T., 2006. The HYDRUS software package for simulating two and three-dimensional movement of water, heat, and multiple solutes in variably-saturated media. Technical Manual, Version 1.0. PC Progress, Prague, Czech Republic.

Šimůnek, J., van Genuchten, M.T., Šejna, M., 2016. Recent developments and applications of the HYDRUS computer software packages. Vadose Zone J. 15 (7). https://doi.org/10.2136/vzj2016.04.0033.

Solangi, G.S., Siyal, A.A., Siyal, P.., 2019. Spatiotemporal dynamics of land surface temperature and its impact on the vegetation. Civil Eng. J. 5 (8), 1753–1763. https://doi.org/10.28991/cej-2019-03091368.

Su, Y., Li, Y., Zhao, H., 2006. Soil properties and their spatial pattern in a degraded sandy grassland under post-grazing restoration, Inner Mongolia, northern China. Biogeochemistry 79 (3), 297–314. https://doi.org/10.1007/s10533-005-5273-1.

Thompson, S., Harman, C.J., Heine, P., Katul, G.G., 2010. Vegetation-infiltration relationships across climatic and soil type gradients. J. Geophys. Res. 115 (G2), G02023. https://doi.org/10.1029/2009JG001134.

Vieira, G., Bockheim, J., Guglielmin, M., Balks, M., Abramov, A.A., Boelhouwers, J., Cannone, N., Ganzert, L., Gilichinsky, D.A., Goryachkin, S., López-Martínez, J., Meiklejohn, I., Raffi, R., Ramos, M., Schaefer, C., Serrano, E., 2010. Thermal state of permafrost and active-layer monitoring in the antarctic: advances during the international polar year 2007–2009. Permafrost periglac 21, 182–197. https://doi.org/10.1002/ppp.685.

Wall, A., Heiskanen, J., 2003. Water-retention characteristics and related physical properties of soil on afforested agricultural land in Finland. For. Ecol. Manag. 186 (1–3), 21–32. https://doi.org/10.1016/S0378-1127(03)00239-1.

Wamelink, G.W.W., van Dobben, H.F., Goedhart, P.W., Jones-Walters, L.M., 2018. The role of abiotic soil parameters as a factor in the success of invasive plant species. Civil Eng. J. 2 (6), 308–365. https://doi.org/10.28991/esj-2018-01155.

Wang, G.X., Wang, Y.B., Li, Y.S., Cheng, H.Y., 2007. Influences of alpine ecosystem responses to climatic change on soil properties on the Qinghai-Tibet Plateau, China. Catena 70 (3), 506–514. https://doi.org/10.1016/j.catena.2007.01.001.

Wang, G.X., Li, Y.S., Wang, Y.B., Wu, Q.B., 2008. Effects of permafrost thawing on vegetation and soil carbon pool losses on the Qinghai-Tibet Plateau, China. Geoderma 143 (1–2), 143–152. https://doi.org/10.1016/j.geoderma.2007.10.023.

Wang, G.X., Hu, H.C., Li, T.B., 2009. The influence of freeze-thaw cycles of active soil layer on surface runoff in a permafrost watershed. J. Hydrol. 375 (3–4), 438–449. https://doi.org/10.1016/j.jhydrol.2009.06.046.

Wang, G.X., Liu, G.S., Liu, C.J., Yang, Y., 2012. The variability of soil thermal and hydrological dynamics with vegetation cover in a permafrost region. Agric. For. Meteorol. 162-163, 0–57. https://doi.org/10.1016/j.agrformet.2012.04.006.

Wang, Y., Niu, F., Wu, Q., Gao, Z., 2014. Assessing soil erosion and control factors by radiometric technique in the source region of the yellow river, Tibetan plateau. Quat. Res. 81 (3), 538–544. https://doi.org/10.1016/j.yqres.2013.11.003.

Wang, Y.S., Cheng, C.C., Xie, Y., Liu, B.Y., Yin, S.Q., Liu, Y.N., et al., 2017. Increasing trends in rainfall-runoff erosivity in the source region of the three Rivers, 1961–2012. Sci. Total Environ. 592, 639–648. https://doi.org/10.1016/j.scitotenv.2017.02.235.

Wang, Y., Sun, Z., Sun, Y., 2018. Effects of a thaw slump on active layer in permafrost regions with the comparison of effects of thermokarst lakes on the Qinghai-Tibet plateau, China. Geoderma 314, 47–57. https://doi.org/10.1016/j.geoderma.2017.10.046.

Weiler, M., Flühler, H., 2004. Inferring flow types from dye patterns in macroporous soils. Geoderma 120 (1–2), 137–153. https://doi.org/10.1016/j.geoderma.2003.08.014.

Wen, L., Dong, S., Zhu, L., Li, X., Shi, J., Wang, Y., Ma, Y., 2010. Change of soil organic carbon density of alpine meadow in the headwater areas of Qinghai-Tibetan Plateau, China. Procedia Environ. Sci. 2, 619–624. https://doi.org/10.1016/j.proenv.2010.10.069.

Wu, Q., Shen, Y., Shi, B., 2003. Relationship between frozen soil together with its water-heat process and ecological environment in the Tibetan Plateau. J. Glaciol. Geocryol. 25 (3), 250–255 (in Chinese). https://doi.org/10.7522/j.issn.1000-0240.2014.0105.

Yan, P., Dong, Z.B., Dong, G.R., Zhang, X.B., Zhang, Y.Y., 2001. Preliminary results of using Cs-137 to study wind erosion in the Qinghai-Tibet Plateau. J. Arid Environ. 47 (4), 443–452. https://doi.org/10.1006/jare.2000.0749.

Yang, Y., Chen, R.S., Song, Y.X., Guo, S.H., Liu, Z.W., Wang, L., 2017. Comparison experimental study on double-ring infiltrometers with different sizes in the Qilian Mountain. J. Soil Water Conserv. 31 (1), 328–336 (in Chinese). 10.13870/j.cnki.stbcxb.2017.01.054.

Yin, G., Niu, F., Lin, Z., Luo, J., Liu, M., 2017. Effects of local factors and climate on permafrost conditions and distribution in Beiluhe basin, Qinghai-Tibet Plateau, China. Sci. Total Environ. 581-582, 472–485. https://doi.org/10.1016/j.scitotenv.2016.12.155.

You, Q.G., Xue, X., Peng, F., Xu, M., Duan, H., Dong, S., 2014. Comparison of ecosystem characteristics between degraded and intact alpine meadow in the Qinghai-Tibetan Plateau, China. Ecol. Eng. 71, 133–143. https://doi.org/10.1016/j.ecoleng.2014.07.022.

Zeng, C., Zhang, F., Wang, Q., Chen, Y., Joswiak, D.R., 2013. Impact of alpine meadow degradation on soil hydraulic properties over the Qinghai-Tibetan Plateau. J. Hydrol. 478 (2), 148–156. https://doi.org/10.1016/j.jhydrol.2012.11.058.

Zhang, W., An, S., Xu, Z., Cui, J., Xu, Q., 2011. The impact of vegetation and soil on runoff regulation in headwater streams on the east Qinghai-Tibet Plateau, China. Catena 87 (2), 182–189. https://doi.org/10.1016/j.catena.2011.05.020.

Zhao, L., Ping, C., Yang, D., Cheng, G., Ding, Y., Liu, S., 2004. Changes of climate and seasonally frozen ground over the past 30 years in Qinghai-Xizang (Tibetan) Plateau, China. Glob. Planet. Chang. 43 (1–2), 19–31. https://doi.org/10.1016/j.gloplacha.2004.02.003.

Zhu, X.A., Chen, C.F., Wu, J.E., Yang, J.B., Zhang, W.J., Zou, X., Liu, W.J., Jiang, X.J., 2019. Can intercrops improve soil water infiltrability and preferential flow in rubber-based agroforestry system? Soil Tillage Res. 191, 327–339. https://doi.org/10.1016/j.still.2019.04.017.